Seismic signatures of two orthogonal sets of vertical microcorrugated fractures

Rodrigo Felício Fuck and Ilya Tsvankin

Center for Wave Phenomena, Department of Geophysics,

Colorado School of Mines, Golden, CO, 80401-1887

(May 25, 2006)

ABSTRACT

Conventional fracture-characterization techniques operate with the idealized model of penny-shaped (rotationally invariant) cracks and ignore the roughness (microcorrugation) of fracture surfaces. Here, we develop analytic solutions based on the linear-slip theory to examine wave propagation through an effective anisotropic medium that contains two microcorrugated, vertical, orthogonal fracture sets in isotropic background rock.

The off-diagonal elements of the compliance matrix associated with the corrugation cause the deviation of the polarization vectors of the vertically traveling S-waves from the horizontal plane. Also, the shear-wave splitting coefficient at vertical incidence becomes sensitive to fluid saturation, especially for tight, low-porosity host rock. In contrast to the model with two orthogonal sets of penny-shaped cracks, the NMO (normal-moveout) ellipses of all three reflection modes (P, S_1, S_2) are rotated

with respect to the fracture strike directions. Another unusual property of the fast shear wave S_1, which can help to distinguish between models with one and two microcorrugated fracture sets, is the misalignment of its polarization vector at vertical incidence and the semi-major axis of the NMO ellipse.

The model analyzed here may adequately describe the orthogonal fracture sets at Weyburn Field in Canada, where the axes of the P-wave NMO ellipse deviate from the S_1-wave polarization direction. Our results can be used to identify the underlying physical model and, potentially, to estimate the combinations of fracture parameters constrained by multicomponent, multiazimuth seismic data.

INTRODUCTION

A key element in reservoir characterization is identification of fluid pathways that control the production of hydrocarbons. Since such pathways are often formed by fracture networks and joints, detection and analysis of fractures using seismic data is an important area of reservoir geophysics (e.g., Lynn et al., 1995; Pérez et al., 1999; Mallick et al., 1998; DeVault et al., 2002). In a series of three papers, Bakulin et al. (2000a,b,c) outlined several practical approaches to estimating fracture parameters from surface seismic and VSP (vertical seismic profiling) data. Using the linear-slip theory described by Schoenberg (1980) and Schoenberg and Sayers (1995), they expressed the equations describing the NMO (normal-moveout) ellipses and AVO (amplitude-variation-with-offset) gradients of reflected waves in terms of the fracture compliances and orientations. These analytic expressions helped Bakulin et al. (2000a,b,c) to devise fracture-characterization methods based on the inversion of multicomponent, mutliazimuth reflection data.

The work of Bakulin et al. (2000a,b,c) was largely focused on the idealized model of rotationally invariant fractures (i.e., oblate spheroids), which have perfectly smooth surfaces and are often called "penny-shaped cracks." Grechka et al. (2003) extended the results of Bakulin et al. (2000a) by considering a single set of the most general vertical fractures allowed by the linear-slip formalism. Physically, such "general" fractures have rough (microcorrugated) surfaces and are described by a compliance matrix that has nonzero off-diagonal elements. The results of Grechka et al. (2003) show that fracture rheology has a strong impact on the velocities and reflection move-

out of pure modes, as well as on the shear-wave splitting coefficient. For instance, if the fractures are rotationally invariant, the axes of the NMO ellipses from horizontal reflectors are always parallel and perpendicular to the fracture strike. By contrast, for a set of general fractures only the NMO ellipse of the fast shear wave S_1 maintains its alignment with the fractures, while the ellipses of the P- and S_2-waves may have different orientations.

While the methodology of Grechka et al. (2003) helps to treat realistic fracture rheologies, their results are limited to effective media that include only one general fracture set. Many naturally fractured reservoirs, however, contain two (or even more) systems of fractures, which are often orthogonal to each other (Schoenberg and Sayers, 1995; Grechka and Tsvankin, 2003). Here, we study an effective anisotropic medium formed by two vertical, orthogonal, microcorrugated fracture sets embedded in isotropic background rock.

Our motivation for investigating this model comes from analysis of multiazimuth P- and S-wave reflection data acquired at Weyburn Field in Canada, where borehole imaging and geological information reveal the presence of three open vertical fracture sets (Cardona, 2002). Over most of the field two of these sets, which have relatively close orientations, seem to act as a single effective fracture set orthogonal to the dominant NE-SW fracture trend. If these two orthogonal sets are rotationally invariant, the effective medium should have orthorhombic symmetry, which is confirmed by analysis of seismic data (Cardona, 2002). In the southern part of the field, however, the orthorhombic model fails to explain the misalignment of the P-wave NMO ellipse

and the fast S-wave polarization direction. As shown by Cardona (2002), even the introduction of a third set of penny-shaped cracks is insufficient to fit the seismic signatures in that area. Making the fractures microcorrugated can help to develop an effective model with two orthogonal fracture sets that fully accounts for the observed anomaly.

The objective of this paper is to analyze the influence of two orthogonal sets of microcorrugated fractures on the NMO ellipses and AVO gradients of reflected waves, as well as on the shear-wave splitting coefficient. Applying the weak-anisotropy approximation, we derive closed-form analytic expressions for these common seismic signatures in terms of the fracture compliances. Although the feasibility study by Grechka and Tsvankin (2003) indicates that the individual compliances of two general fracture sets cannot be resolved even from the complete effective stiffness tensor, our results can assist in retrieving certain combinations of the compliances and identifying the presence of two fracture sets.

EFFECTIVE MEDIUM

The model considered here includes two orthogonal sets of vertical fractures of the most general rheology embedded in a purely isotropic background (Figure 1). To compute the elastic stiffnesses for the fractured model, we employ the linear-slip theory introduced by Schoenberg (1980) and further discussed by Schoenberg and Sayers (1995) and others (see Appendix A). According to the linear-slip formalism, fractures can be described as non-welded interfaces that cause discontinuities in the displace-

ment field (i.e., slips). The slips are taken to be proportional to the product of the (continuous) tractions that act across the fractures and the excess fracture compliances.

The most general mathematical description of a fracture set in the linear-slip theory is a 3×3 symmetric matrix of the excess compliances (Grechka et al., 2003):

$$\mathbf{K} = \begin{pmatrix} K_N & K_{NH} & K_{NV} \\ K_{NH} & K_H & K_{VH} \\ K_{NV} & K_{VH} & K_V \end{pmatrix}, \tag{1}$$

where K_N is the normal compliance that relates the normal traction (stress) across the fracture surface to the normal slip, and K_V and K_H are the tangential compliances relating the shear stresses to the tangential slips. The off-diagonal compliances incorporate the mechanical effects of irregularities and asperities on the fracture surfaces (Figure 2) by coupling the normal slips to the shear stresses and vice versa (Schoenberg and Douma, 1988). Due to lack of experimental data on this coupling mechanism (with the exception of Nakagawa et al., 2000), it is unclear what scale of microcorrugations is needed to produce measurable off-diagonal compliances. As follows from the theoretical analysis of Kachanov and Sevostianov (2005), microcorrugations should be mismatched and should provide contact points between the two fracture surfaces to ensure significant coupling.

Fractures are usually classified in accordance with the structure of their compliance matrix $\mathbf{K}$ (equation 1). If at least one of the off-diagonal elements does not vanish, the fractures are sometimes called "monoclinic" (Schoenberg and Douma, 1988).

Fractures described by a diagonal matrix $\mathbf{K}$ are called "orthotropic" or simply "diagonal;" rotationally invariant fractures are a special subset of diagonal fractures corresponding to equal tangential compliances $K_V = K_H$.

In the linear-slip theory, the compliance matrix of the effective model is obtained by adding the compliance matrices of the two corrugated fracture sets to that of the isotropic background (Appendix A). The effective stiffness elements c_{ij}, obtained by inverting the compliance matrix, can be simplified by linearizing the exact values in the normalized compliances called fracture weaknesses (Schoenberg and Douma, 1988; Bakulin et al., 2000a). The weaknesses vary from zero for unfractured medium to unity for intensely fractured rock in which the body-wave velocities go to zero in a certain direction. Since the weaknesses for typical fractured formations are much smaller than unity, they can be conveniently used in developing closed-form approximations for seismic signatures. The fracture weaknesses Δ_N, Δ_V, Δ_H, Δ_{NV}, Δ_{NH}, and Δ_{VH} for our model are defined in equations B-1–B-6.

The effective stiffness matrix linearized in the weaknesses of both fracture sets can be represented as (see Appendix B)

$$\mathbf{c} = \begin{pmatrix} c_{11} & c_{12} & c_{13} & \chi c_{24} & c_{15} & c_{16} \\ c_{12} & c_{22} & c_{23} & c_{24} & \chi c_{15} & c_{26} \\ c_{13} & c_{23} & c_{33} & \chi c_{24} & \chi c_{15} & c_{36} \\ \chi c_{24} & c_{24} & \chi c_{24} & c_{44} & 0 & c_{46} \\ c_{15} & \chi c_{15} & \chi c_{15} & 0 & c_{55} & c_{56} \\ c_{16} & c_{26} & c_{36} & c_{46} & c_{56} & c_{66} \end{pmatrix}, \tag{2}$$

where

$$\chi \equiv \frac{\lambda}{(\lambda + 2\mu)} .$$

The linearized stiffnesses c_{ij} are given in equations B-10–B-30. According to equation 2, the effective model has the most general, triclinic symmetry (i.e., it does not have symmetry planes or axes of rotational symmetry), with only one vanishing elastic constant, $c_{45} = c_{54}$. This is not surprising since even a single set of microcorrugated fractures creates an effective triclinic medium. Nonetheless, only 14 out of the 20 elastic constants are independent because the effective model is constructed using the two Lamé parameters of the isotropic background (λ and μ) and 12 fracture compliances (six for each fracture set). Note that if the fracture azimuth is unknown, it is also necessary to introduce an orientation angle that defines the azimuth of one of the sets in a specified coordinate frame.

By dividing the matrix $\mathbf{c}$ into 3×3 submatrices $\mathbf{c}_i$, it can be represented in block form:

$$\mathbf{c} = \left(\begin{array}{c|c} \mathbf{c}_1 & \mathbf{c}_2 \\ \hline \mathbf{c}_2^T & \mathbf{c}_3 \end{array} \right) ; \tag{3}$$

the superscript "T" denotes transposition. The influence of the complex fracture rheology in our model on the structure of the stiffness matrix can be understood by comparing the matrix 3 with that for an effective orthorhombic medium due to two orthogonal sets of rotationally invariant fractures (Bakulin et al., 2000b):

$$\mathbf{c}^{\mathrm{orth}} = \left(\begin{array}{c|c} \mathbf{c}_1^{\mathrm{orth}} & \mathbf{0} \\ \hline \mathbf{0} & \mathbf{c}_3^{\mathrm{orth}} \end{array} \right) . \tag{4}$$

Clearly, the block $\mathbf{c}_2$ vanishes if the fractures are rotationally invariant. Note that the matrix $\mathbf{c}_3^{\text{orth}}$ in equation 4 is diagonal, and c_{66} contained in $\mathbf{c}_3^{\text{orth}}$ is a linear combination of c_{44} and c_{55}.

VERTICAL WAVE PROPAGATION

Approximate velocities and polarizations

The phase velocities and polarization vectors of vertically propagating plane waves can be obtained by solving the Christoffel equation for the effective medium described by the stiffness matrix 2. Applying the first-order perturbation theory (e.g., Jech and Pšenčik, 1989; Pšenčik and Vavryčuk, 2002) and linearizing the vertical velocities of the P-, S_1-, and S_2-waves in the weaknesses yields

$$V_P = V_{Pb}\left[1 - \frac{1}{2}\left(\Delta_{N_1} + \Delta_{N_2}\right)\chi^2\right], \tag{5}$$

$$V_{S1} = V_{Sb}\left(1 - \frac{\Delta_{V_2}}{2}\right), \tag{6}$$

$$V_{S2} = V_{Sb}\left(1 - \frac{\Delta_{V_1}}{2}\right), \tag{7}$$

where V_{Pb} and V_{Sb} are the P- and S-wave velocities in the isotropic background, whereas Δ_{N_i} and Δ_{V_i} denote the normal and vertical weaknesses of fracture sets 1 and 2, as indicated by the subscript i. It is assumed that the first set has a larger weakness Δ_V than the second set; otherwise, equation 6 for V_{S1} would give the vertical velocity of the slow S-wave. Although the vertical velocities are influenced by the presence of fractures, equations 5–7 do not contain off-diagonal weaknesses and,

therefore, coincide with the linearized velocities for rotationally invariant fractures (Bakulin et al., 2000b).

In contrast, the polarization vectors ($\mathbf{U}$) of the vertically traveling waves contain first-order contributions of the off-diagonal compliances Δ_{NV_i}:

$$\mathbf{U}_P \approx (a\,\Delta_{NV_1},\, a\,\Delta_{NV_2},\, 1)^T \ , \tag{8}$$

$$\mathbf{U}_{S1} \approx (0, 1,\, -a\,\Delta_{NV_2})^T \ , \tag{9}$$

$$\mathbf{U}_{S2} \approx (1, 0,\, -a\,\Delta_{NV_1})^T \ , \tag{10}$$

where

$$a \equiv \frac{(1-2g_b)}{(1-g_b)}\sqrt{g_b} \ , \qquad g_b \equiv \left(\frac{V_{Sb}}{V_{Pb}}\right)^2 .$$

Because of the corrugation of fracture surfaces, the P-wave polarization vector deviates from the vertical, and the vertically propagating shear waves are no longer polarized in the horizontal plane. Equations 9 and 10, however, show that the shear-wave polarization vectors are still confined to the planes of the two fracture sets.[1]

Therefore, Alford-style rotation of the horizontal displacement components of near-offset S-wave reflections can be used to estimate the fracture azimuths. To measure the vertical components of the shear-wave polarization vectors, which are indicative of the presence of microcorrugated fractures, it is necessary to apply 3D polarization analysis.

[1]Due to the limitations of the first-order perturbation theory, the shear-wave polarization vectors are no longer orthogonal, despite being perpendicular to the P-wave polarization vector. Also, the perturbed polarization vectors were not normalized; still, to the first order in the fracture weaknesses, the magnitude of the vectors $\mathbf{U}_P$, $\mathbf{U}_{S1}$ and $\mathbf{U}_{S2}$ is equal to unity.

Shear-wave splitting

The shear-wave splitting coefficient (γ^S) at vertical incidence is defined as (Thomsen, 1988; Tsvankin, 2001)

$$\gamma^S \equiv \frac{V_{S1}^2 - V_{S2}^2}{2V_{S2}^2}\,, \tag{11}$$

where V_{S1} is the velocity of the fast shear wave. Applying the second-order perturbation theory (Farra, 2001) and retaining terms quadratic in the fracture weaknesses, we find

$$\begin{aligned}\gamma^S =& \frac{1}{2}\Bigg\{ \left(\Delta_{V_1} - \Delta_{V_2}\right)\left(1 + \Delta_{V_1} - \Delta_{V_2}\right) \\ & - g_b\left[\left(\Delta_{VH_1}^2 - \Delta_{VH_2}^2\right) + \left(\Delta_{NV_1}^2 - \Delta_{NV_2}^2\right)\frac{(3-4g_b)}{1-g_b}\right]\Bigg\}\,.\end{aligned} \tag{12}$$

As expected, γ^S at vertical incidence vanishes when the two fracture sets have identical weaknesses. If the terms quadratic in the weaknesses are dropped from equation 12, the splitting coefficient reduces to the difference between the diagonal tangential weaknesses Δ_{V_1} and Δ_{V_2} (see equations 6 and 7). Therefore, to the first order γ^S coincides with the splitting coefficient for rotationally invariant fractures, which is controlled by the difference between the fracture densities of the two sets (Thomsen, 1988; Bakulin et al., 2000a,b).

However, if the second-order terms are substantial, γ^S is also influenced by the off-diagonal weaknesses Δ_{VH_i} and Δ_{NV_i}. Note that the weakness Δ_{NV_i} depends on saturation and takes different values for fractures filled with compressible gas, brine,

or oil (Bakulin et al., 2000c).[2] Therefore, the vertical-incidence splitting coefficient for microcorrugated fractures with relatively large off-diagonal weaknesses may serve as an indicator of fluid saturation.

As illustrated by Figure 3, the exact coefficient γ^S can vary by as much as 50% over the entire range of plausible values of Δ_{NV_1} (Δ_{NV_2} was fixed). We would like to emphasize that the exact γ^S (as well as the exact NMO ellipses below) is computed from the exact (not linearized) stiffness matrix for our model obtained using the linear-slip theory (see Appendix A). For a tight (non-porous) host rock, $\Delta_{NV_1} = 0$ corresponds to fractures filled with incompressible fluid such as brine, whereas nonzero values of Δ_{NV_1} describe fractures at least partially saturated with gas (Bakulin et al., 2000c). Although the weak-anisotropy approximation 12 correctly reproduces the overall character of the curve $\gamma^S(\Delta_{NV_1})$, it understimates the sensitivity of the shear splitting to the weakness Δ_{NV_1}.

If the saturation of both both fracture sets changes simultaneously and Δ_{NV_2} varies similarly to Δ_{NV_1}, the splitting coefficient becomes less sensitive to fluid content. Also, when the host rock has pore space hydraulically connected to the fractures, the weaknesses Δ_{NV_i} do not necessarily vanish even for incompressible saturating fluids (Cardona, 2002; Gurevich, 2003). As a consequence, for porous rocks the variation of γ^S with saturation may be less pronounced than that suggested by Figure 3. Finally, γ^S becomes less sensitive to the off-diagonal compliances and saturation for softer

[2]Equation 12 is more accurate than equation (30) of Bakulin et al. (2000c) because it includes all terms quadratic in the weaknesses.

rocks (e.g., marine sediments) with smaller values of the ratio g_b , i.e., higher V_P/V_S ratios.

NMO ELLIPSES FROM HORIZONTAL REFLECTORS

Important information for fracture detection is provided by azimuthally varying traveltimes (moveout) of reflected waves, in particular by their normal-moveout (NMO) ellipses. For a horizontal, homogeneous layer of arbitrary anisotropic symmetry, the NMO velocity of pure (non-converted) reflection modes as a function of the azimuth α is given by (Grechka et al., 1999):

$$V_{\rm nmo}^{-2} = W_{11}\cos^2\alpha + 2W_{12}\sin\alpha\cos\alpha + W_{22}\sin^2\alpha\,, \tag{13}$$

where $\mathbf{W}$ is a symmetric 2×2 matrix,

$$\mathbf{W} = \frac{q}{q_{,12}^2 - q_{,11}q_{,22}} \begin{pmatrix} q_{,22} & -q_{,12} \\ -q_{,12} & q_{,11} \end{pmatrix}. \tag{14}$$

Here, q is the vertical component of the slowness vector $\mathbf{p} = [p_1, p_2, q]$ of the zero-offset ray and $q_{,ij}$ denote the following partial derivatives evaluated at zero offset:

$$q_{,ij} \equiv \frac{\partial^2 q(p_1,p_2)}{\partial p_i \partial p_j}\,. \tag{15}$$

The vertical slowness and its derivatives can be obtained from the Christoffel equation, as discussed by Grechka et al. (1999). If the eigenvalues of the matrix $\mathbf{W}$ are positive (the most typical case), equation 13 describes an ellipse in the horizontal plane.

To analyze the dependence of the NMO ellipses on the medium parameters, it is convenient to linearize equation 14 in the fracture weaknesses (equations B-1–B-6). For P-waves, the linearized matrix $\mathbf{W}$ takes the form

$$\mathbf{W}^P = \frac{1}{V_{Pb}^2} \begin{pmatrix} W_{11}^P & W_{12}^P \\ W_{12}^P & W_{22}^P \end{pmatrix}, \tag{16}$$

where

$$W_{11}^P = 1 + \Delta_{N_1} \left(1 - 4g_b^2\right) + \Delta_{N_2} \left(1 - 2g_b\right)^2 + 4g_b \, \Delta_{V_1}, \tag{17}$$

$$W_{12}^P = 2 \left(\Delta_{NH1} + \Delta_{NH_2}\right) \left(1 - 2g_b\right) \sqrt{g_b}, \tag{18}$$

$$W_{22}^P = 1 + \Delta_{N_2} \left(1 - 4g_b^2\right) + \Delta_{N_1} \left(1 - 2g_b\right)^2 + 4g_b \, \Delta_{V_2}. \tag{19}$$

The structure of equations 17–19 can be understood from the "addition rule" formulated by Bakulin et al. (2000b). To find the linearized weak-anisotropy approximation for most seismic signatures (one exception is discussed below), the anisotropic terms due to each fracture set can be simply added together taking into account the fracture orientation. This recipe can be used to obtain equations 17–19 from the P-wave NMO ellipse for a single set of microcorrugated fractures given in equation (56) of Grechka et al. (2003).

For the fast shear wave S_1 the matrix $\mathbf{W}$ becomes

$$\mathbf{W}^{S1} = \frac{1}{V_{Sb}^2} \begin{pmatrix} W_{11}^{S1} & W_{12}^{S1} \\ W_{12}^{S1} & W_{22}^{S1} \end{pmatrix}, \tag{20}$$

with

$$W_{11}^{S1} = 1 + \Delta_{H_1} + \Delta_{H_2} - \mathcal{A}\,, \tag{21}$$

$$W_{12}^{S1} = \sqrt{g_b}\,\left(2\Delta_{NH_2} - \mathcal{C}\right), \tag{22}$$

$$W_{22}^{S1} = 1 - 3\Delta_{V_2} + 4g_b\,\Delta_{N_2} - \mathcal{B}\,. \tag{23}$$

Here,

$$\mathcal{A} \equiv \mathcal{D}\,\Delta_{VH_1}^2\,, \tag{24}$$

$$\mathcal{B} \equiv \mathcal{D}\,\Delta_{VH_2}^2\,, \tag{25}$$

$$\mathcal{C} \equiv \mathcal{D}\,\Delta_{VH_1}\,\Delta_{VH_2}\,, \tag{26}$$

and

$$\mathcal{D} \equiv \frac{g_b}{(\Delta_{V_1} - \Delta_{V_2})}\,. \tag{27}$$

Although the factors $\mathcal{A}$, $\mathcal{B}$, and $\mathcal{C}$ are proportional to products of the weaknesses Δ_{VH_i}, their denominator contains the difference in the tangential weaknesses Δ_{V_i} (see equation 27). For that reason, $\mathcal{A}$, $\mathcal{B}$, and $\mathcal{C}$ have to be retained in the linearized approximation for the NMO ellipse $\mathbf{W}^{S1}$. In such a case, the addition rule discussed above is not valid, and the approximate NMO ellipse of the S_1-wave cannot be obtained as the sum of the contributions of each fracture set.

The linearized matrix $\mathbf{W}$ for the S_2-wave is given by

$$\mathbf{W}^{S2} = \frac{1}{V_{Sb}^2}\begin{pmatrix} W_{11}^{S2} & W_{12}^{S2} \\ W_{12}^{S2} & W_{22}^{S2} \end{pmatrix}, \tag{28}$$

where

$$W_{11}^{S2} = 1 - 3\Delta_{V_1} + 4g_b\,\Delta_{N_1} + \mathcal{A}\,, \tag{29}$$

$$W_{12}^{S2} = \sqrt{g_b}\,\left(2\Delta_{NH_1} + \mathcal{C}\right), \tag{30}$$

$$W_{22}^{S2} = 1 + \Delta_{H_1} + \Delta_{H_2} + \mathcal{B}\,. \tag{31}$$

Equations 16–31 show that only the presence of the off-diagonal weaknesses can explain the misalignment of the NMO ellipses with the fracture planes. If both fracture sets were rotationally invariant, the matrices $\mathbf{W}$ for all three modes (equations 16, 20, and 28) would be diagonal, and the axes of the NMO ellipses would be parallel to the fracture strike directions. In an effective orthorhombic medium due to two orthogonal sets of rotationally invariant fractures, the semi-major axes of the NMO ellipses of the P- and S_1-waves (Figure 4) are aligned with the strike of the dominant fracture set (Bakulin et al., 2000b).

By contrast, when both fracture sets are microcorrugated, all three NMO ellipses generally have different orientations, and none of them is aligned with the fracture azimuths (Figure 5). The deviation of the semi-major axis of the NMO ellipse from the azimuth of the dominant fracture set reaches 30° for the P-wave and 20° for the S_1-wave. The weak-anisotropy approximations for the NMO ellipses are close to the exact solutions for the full range of azimuths (Figure 6). The error of the approximate solution, caused primarily by the misalignment of the axes of the exact and approximate NMO ellipses, is noticeable only for the slow shear wave S_2. The higher accuracy of the approximation for the S_1-wave compared to that for the S_2-

wave is not surprising since equations 22 and 23 for the matrix elements W_{12}^{S1} and W_{22}^{S1} become exact for one set of fractures (Grechka et al., 2003).

The orientation of the NMO ellipse of the fast wave S_1 can help to distinguish between the models with one or two microcorrugated fracture sets. If the second set does not exist, then $\Delta_{NH_2} = \Delta_{VH_2} = 0$, and the element W_{12} for the S_1-wave vanishes (equations 22 and 26). In this case, the matrix $\mathbf{W}^{S1}$ (equation 20) becomes diagonal, and the semi-major axis of the NMO ellipse of the S_1-wave is parallel to both the fast shear-wave polarization direction (equation 9) and the fracture strike. Moreover, for the model with one set of microcorrugated fractures, both the S_1-wave vertical velocity and the NMO velocity in the fracture-strike direction coincide with the background velocity V_{Sb}. This result, discussed by Grechka et al. (2003), follows from equations 6, 20, and 23.

Grechka et al. (2000) defined the Thomsen-style parameters $\zeta^{(i)}$ $(i = 1, 2, 3)$ responsible for the orientations of the NMO ellipses of pure modes in a horizontal monoclinic layer with a horizontal symmetry plane. Equations 16–31 can be used to generalize their result for our triclinic model because the elements W_{12} include the parameters $\zeta^{(i)}$ and, for the shear waves, additional correction terms. Using equations B-21 and B-24, the element W_{12}^P (equation 18) responsible for the rotation of the P-wave NMO ellipse with respect to the x_1-axis can be represented as

$$W_{12}^P = -2\frac{c_{36}}{c_{33}} = -2\zeta^{(3)}, \tag{32}$$

which coincides with the expression for W_{12}^P in Grechka et al. (2000). For our model, the parameter $\zeta^{(3)}$ is proportional to the sum of the weaknesses Δ_{NH_1} and Δ_{NH_2}.

Similarly, the off-diagonal elements W_{12}^{S1} and W_{12}^{S2} for the S-waves (equations 22 and 30) can be expressed through the parameters $\zeta^{(1)}$ and $\zeta^{(2)}$:

$$W_{12}^{S1} = -2\,\frac{c_{16} - c_{36}}{2V_{Pb}^2\, g_b} + \mathcal{C} = -2\frac{\zeta^{(1)}}{g_b} + \mathcal{C}\,, \tag{33}$$

$$W_{12}^{S2} = -2\,\frac{c_{26} - c_{36}}{2V_{Pb}^2\, g_b} - \mathcal{C} = -2\frac{\zeta^{(2)}}{g_b} - \mathcal{C}\,, \tag{34}$$

where $\mathcal{C}$ (equation 26) is an additional correction factor needed to account for the nonzero stiffnesses c_{46} and c_{56} in the triclinic model (equation 3). The parameters $\zeta^{(1)}$ and $\zeta^{(2)}$ depend on the weaknesses Δ_{NH_2} and Δ_{NH_1}, respectively.

Our approximations for the NMO ellipses of both S-waves break down when tangential weaknesses Δ_{V_1} and Δ_{V_2} are identical and the weaknesses $\Delta_{VH_i} \neq 0$. In this case, the parameter $\mathcal{D}$ (equation 27) goes to infinity, which reflects the fact that a point shear-wave singularity develops in a close vicinity of the zero-offset ray. Analysis of the influence of singularities on normal moveout for models with two orthogonal sets of penny-shaped cracks can be found in Bakulin et al. (2000b).

P-WAVE REFLECTION COEFFICIENT

Another seismic signature that can be effectively used in fracture detection is the azimuthally varying reflection coefficient, in particular the AVO (amplitude variation with offset) gradient responsible for small- and moderate-offset reflection amplitudes. Here, we present a linearized expression for the P-wave AVO response in our model and discuss its dependence on the fracture weaknesses.

We consider an isotropic incidence halfspace separated by a plane boundary from

the triclinic medium described by equation 2 and assume a weak contrast in the elastic properties across the interface and weak anisotropy in the reflecting halfspace (i.e., the triclinic medium is treated as a perturbation of the incidence isotropic medium caused by small fracture weaknesses). The weak-contrast, weak-anisotropy approximation for the P-wave reflection coefficient in arbitrary anisotropic media is derived in Vavryčuk and Pšenčik (1998). By combining their general result with the linearized stiffness coefficients for our model (equations B-10–B-30), we find the P-wave reflection coefficient R_{PP} as a function of the phase incidence angle θ:

$$\begin{aligned} R_{PP} &= A + B\sin^2\theta + C\sin^2\theta\,\tan^2\theta \\ &= A_{\text{iso}} + A_{\text{ani}} + (B_{\text{iso}} + B_{\text{ani}})\sin^2\theta + (C_{\text{iso}} + C_{\text{ani}})\sin^2\theta\tan^2\theta\,. \end{aligned} \tag{35}$$

Here, A is the normal-incidence reflection coefficient ("AVO intercept"), B is the AVO gradient, and C is the so-called "curvature" (large-angle) term. In the weak-contrast, weak-anisotropy approximation, each term can be separated into the isotropic (subscript "iso") and anisotropic (subscript "ani") part. Since the isotropic part of the linearized reflection coefficient is well known (it is expressed through the background velocities and densities), we will discuss only the additional anisotropic terms. The anisotropic component of the AVO intercept A is formed by the contribution of the normal fracture weaknesses to the P-wave vertical velocity in the fractured layer:

$$A_{\text{ani}} = -\frac{(\Delta_{N_1} + \Delta_{N_2})\,\chi^2}{4}\,. \tag{36}$$

The anisotropic part of the AVO gradient is given by

$$B_{\text{ani}}(\phi) = A_{\text{ani}} + B_1 \cos^2\phi + B_2 \sin 2\phi + B_3 \sin^2\phi\,, \tag{37}$$

where ϕ is the azimuthal phase angle measured from the x_1-axis, and

$$B_1 = g_b\big(\Delta_{V_1} - \Delta_{N_1}\chi\big)\,, \tag{38}$$

$$B_2 = -\frac{\chi\sqrt{g_b}}{2}\left(\Delta_{NH_1} + \Delta_{NH_2}\right)\,, \tag{39}$$

$$B_3 = g_b\big(\Delta_{V_2} - \Delta_{N_2}\chi\big). \tag{40}$$

The anisotropic curvature term is obtained as

$$\begin{aligned} C_{\text{ani}}(\phi) = {} & A_{\text{ani}} + C_1 \cos^4\phi + C_2 \sin^4\phi \\ & + \big(C_3 \cos^2\phi + C_4 \sin 2\phi + C_5 \sin^2\phi\big) \sin 2\phi\,, \end{aligned} \tag{41}$$

with

$$C_1 = g_b\,(1 - g_b)\,\Delta_{N_1}, \tag{42}$$

$$C_2 = g_b\,(1 - g_b)\,\Delta_{N_2}, \tag{43}$$

$$C_3 = \frac{\sqrt{g_b}}{2}\big(\Delta_{NH_1} + \Delta_{NH_2}\chi\big), \tag{44}$$

$$C_4 = \frac{\sqrt{g_b}}{4}\left[\Delta_{H_1} + \Delta_{H_2} + \left(\Delta_{N_1} + \Delta_{N_2}\right)\chi\right], \tag{45}$$

$$C_5 = \frac{\sqrt{g_b}}{2}\big(\Delta_{NH_1}\chi + \Delta_{NH_2}\big). \tag{46}$$

There are interesting similarities between equations 37–46 and equations 16–19 for the P-wave NMO ellipse. First, if the sign of the AVO gradient does not change with azimuth, $|B_{\text{ani}}(\phi)|$ plotted as the radius-vector traces out a curve close to an ellipse in the horizontal plane, with $B_{\text{ani}}^{-2}(\phi)$ being exactly elliptical. (Note that the shape of

the azimuthally varying curvature term is more complicated and is not represented by a quadratic function in the horizontal coordinates.) Second, the only off-diagonal weaknesses appearing in the linearized equations for both the reflection coefficient and NMO ellipse are Δ_{NH_1} and Δ_{NH_2}. Third, the "principal directions" of the curve $|B_{\text{ani}}(\phi)|$ are are rotated with respect to the horizontal coordinate axes (i.e., with respect to the fracture azimuths) only when $\Delta_{NH_1} \neq 0$ or $\Delta_{NH_2} \neq 0$. Furthermore, the rotation angle of both the NMO ellipse (equation 18) and AVO gradient (equation 39) is controlled by the sum $\Delta_{NH_1} + \Delta_{NH_2}$. As shown above, the rotation angle can be also expressed through the anisotropy coefficient $\zeta^{(3)}$ (equation 32).

The example in Figure 7 illustrates the orientation and shape of the magnitude of the azimuthally varying AVO gradient from equation 37. The curve $|B_{\text{ani}}(\phi)|$ ($B_{\text{ani}} < 0$) is close to an ellipse with the semi-major axis deviating by about 55° from the strike of the dominant fracture set. If the weaknesses Δ_{NH_1} and Δ_{NH_2} are set to zero, the direction of the largest (by absolute value) AVO gradient is perpendicular to the dominant fracture set.

Despite the small value of $\Delta_{NH_1} = 0.05$, the contribution of the off-diagonal weaknesses is sufficient for rotating this direction by about 35°. This high sensitivity of the orientation of the AVO-gradient curve to the off-diagonal terms is explained by equations 38–40. While the element B_2 is a weighted average of the weaknesses Δ_{NH_j} ($j = 1, 2$), the coefficients B_1 and B_3 are proportional to the difference $\Delta_{V_i} - \Delta_{N_i}\chi$. Since for our model this difference is small, it does not take large off-diagonal weaknesses to cause a significant rotation of the AVO gradient.

DISCUSSION AND CONCLUSIONS

We studied seismic signatures of an effective medium formed by two sets of vertical, orthogonal fractures with microcorrugated surfaces embedded in isotropic host rock. Each fracture set is described by the most general compliance matrix allowed within the framework of the linear-slip theory, with the off-diagonal compliance elements responsible for the character and degree of corrugation. The effective model is triclinic and has no symmetry planes, although only 15 stiffness elements are independent.

By applying expansions in the fracture weaknesses (normalized compliances), we derived closed-form analytic expressions for shear-wave splitting, the NMO ellipses of horizontal reflection events, and the P-wave reflection coefficient. These weak-anisotropy approximations provide valuable insight into the influence of the fracture rheology on seismic signatures commonly used in reservoir characterization. For instance, the presence of the off-diagonal weaknesses makes the shear-wave splitting coefficient γ^S at vertical incidence sensitive (to the second order) to fluid saturation. The variation of γ^S with saturation may be substantial in tight, high-velocity formations where fluids cannot easily move from the fractures into pore space.

The fracture weaknesses also control the orientation and eccentricity of the NMO ellipses of the reflected P-, S_1, and S_2-waves. In particular, the contributions of the off-diagonal weaknesses Δ_{NH_i} and $\Delta_{VH_i}\,(i = 1, 2)$ lead to the rotation of the NMO ellipses with respect to the fracture strike directions. In contrast to the effective orthorhombic medium formed by two orthogonal sets of penny-shaped cracks, all

three NMO ellipses in our model have different orientations. Extending existing results for monoclinic models, we expressed the rotation angles of the NMO ellipses in triclinic media through the anisotropy parameters $\zeta^{(1)}$, $\zeta^{(2)}$, and $\zeta^{(3)}$.

Analysis of the NMO ellipse of the fast shear wave S_1 suggests a simple way to distinguish between models with one and two microcorrugated fracture sets. For a single set of fractures, the semi-major axis of the S_1-wave NMO ellipse and the polarization vector of the S_1-wave at vertical incidence are parallel to each other and to the fracture strike. This is no longer the case for the model with two fracture sets where the angle between the polarization vector and the semi-major axis of the NMO ellipse for the S_1-wave can reach 20-30°.

For P-waves, the principal azimuthal directions of both the NMO ellipse and AVO gradient depend on the sum of the off-diagonal weaknesses Δ_{NH_1} and Δ_{NH_2}. If both Δ_{NH_1} and Δ_{NH_2} vanish, then the NMO ellipse and AVO gradient are aligned with the fracture strike directions, as is always the case for penny-shaped cracks. Whereas the azimuthally varying P-wave AVO gradient traces out a quasi-elliptical curve (if it does not change sign with azimuth), the large-angle AVO term has a much more complicated azimuthal dependence.

The results of this work can be instrumental in developing inversion algorithms for estimating the fracture parameters from multicomponent seismic data. Unfortunately, it has been shown that the inversion for all 15 independent parameters of this model is ill-posed. Even if all 21 elastic constants of the triclinic medium are recovered with high accuracy, it is impossible to resolve the fracture weaknesses individually.

The equations presented here, however, can help to estimate certain parameter combinations and verify whether the underlying physical model is appropriate. Lack of data on the magnitude of the off-diagonal weaknesses for natural fracture networks makes such experimental studies particularly important.

As discussed above, comparison of the NMO ellipse and polarization direction of the S_1-wave makes it possible to discriminate between the effective models with one and two sets of microcorrugated fractures. Our results also indicate that it may be possible to invert seismic data for the velocity ratio g_b and the differences between the diagonal weaknesses Δ_{N_i}, Δ_{V_i} and Δ_{H_i} of the two sets, if the vertical velocities are available. Also, the P-wave ellipses and AVO gradient can potentially constrain the sum of the off-diagonal weaknesses Δ_{NH_i}.

The weaknesses Δ_{NV_i} do not appear in the linearized equations for any of the NMO ellipses or for the P-wave AVO gradient and contribute only to the second-order term in the shear-wave splitting coefficient. The only quantities that contain first-order contributions of Δ_{NV_i} are the vertical components of the S-wave polarization vectors, which may be difficult to measure on field data. Likewise, the weaknesses Δ_{VH_i} are contained only in relatively small terms in the equations for the shear-wave NMO ellipses and for the splitting coefficient γ^S. Therefore, estimation of the weaknesses Δ_{VH_i} and Δ_{NV_i} is likely to be unstable. For a single microcorrugated fracture set, both Δ_{VH} and Δ_{NV} can be determined from VSP data using the slowness surface of P-waves. It is not clear, however, if such an algorithm can be extended to the more complicated model treated here.

ACKNOWLEDGMENTS

We are grateful to members of the A(nisotropy)-Team of the Center for Wave Phenomena (CWP) at Colorado School of Mines (CSM) for helpful discussions and to Tom Davis and Ken Larner (both CSM) for their reviews of the manuscript. Rodrigo Fuck's graduate studies at CSM were funded by the Brazilian government through CAPES under the scholarship BEX1340-0/00. This work was also supported by the Consortium Project on Seismic Inverse Methods for Complex Structures at CWP and by the Chemical Sciences, Geosciences and Biosciences Division, Office of Basic Energy Sciences, U.S. Department of Energy.

APPENDIX A

ELEMENTS OF THE LINEAR-SLIP THEORY

The linear-slip theory (Schoenberg, 1980; Schoenberg and Sayers, 1995) is designed to find an equivalent (long-wavelength) representation of a medium that contains one or several fracture sets. Fractures are treated as planar and parallel surfaces of weakness, and it is assumed that interaction between fractures can be ignored. The fracture length is taken to be infinite, while fracture apertures have to be small compared to the dominant seismic wavelength. According to the linear-slip theory, the jumps in the displacement vector $[u_i]$ (i.e., "slips") across a fracture are to the first order

proportional to the (continuous) stresses σ_{jk}:

$$[u_i] = h\, K_{ij}\, \sigma_{jk}\, n_k, \tag{A-1}$$

where $\mathbf{n}$ is the normal to the fracture plane, h is the average spacing between fractures, and K_{ij} are called the "compliances" of the fracture set.

The effective compliance tensor $\mathbf{s}$ of a fractured medium is then found as the sum of the background compliance $\mathbf{s}_b$ and the excess compliances $\mathbf{s}_{f_i}$ of all fracture sets (e.g., Schoenberg and Muir, 1989; Hood, 1991):

$$\mathbf{s} = \mathbf{s}_b + \sum_{i=1}^{N} \mathbf{s}_{f_i}. \tag{A-2}$$

The compliances K_{ij} of each fracture set are mapped onto the corresponding compliance tensor s_{ijkl} using Hooke's law (Sayers and Kachanov, 1995):

$$s_{ijkl} = \frac{1}{4}\left(K_{ik}n_l n_j + K_{jk}n_i n_l + K_{il}n_j n_k + K_{jl}n_i n_k\right). \tag{A-3}$$

Equation A-1 indicates that $\mathbf{K}$ is a 3×3 matrix that has to be symmetric and nonnegative definite because of the symmetries of the compliance tensor. Hence, a fracture system can be described by up to six independent compliance elements. The diagonal terms of the matrix relate the jumps in the normal displacement ("normal slips") to the normal tractions acting across the surface of the fractures, as well as the tangential slips to the shear stresses. The off-diagonal elements are responsible for the coupling of the normal slips and shear stresses and vice-versa. Hereafter, we

follow the notation of Grechka et al. (2003):

$$K_{11} \rightarrow K_N; \qquad K_{22} \rightarrow K_H; \qquad K_{33} \rightarrow K_V;$$

$$K_{12} \rightarrow K_{NH}; \qquad K_{13} \rightarrow K_{NV}; \qquad K_{23} \rightarrow K_{VH}.$$

We consider two vertical, orthogonal fracture sets oriented in such a way that that the x_1-axis is perpendicular to the first set. The summation in equation A-2 is more conveniently carried out using the condensed Voigt notation, which allows the compliance tensor to be replaced by a 6×6 compliance matrix. Then, according to equation A-3, the compliances matrices for the two sets take the form

$$s_{f1} = \begin{pmatrix} K_{N_1} & 0 & 0 & 0 & K_{NV_1} & K_{NH_1} \\ 0 & 0 & 0 & 0 & 0 & 0 \\ 0 & 0 & 0 & 0 & 0 & 0 \\ 0 & 0 & 0 & 0 & 0 & 0 \\ K_{NV_1} & 0 & 0 & 0 & K_{V_1} & K_{VH_1} \\ K_{NH_1} & 0 & 0 & 0 & K_{VH_1} & K_{H_1} \end{pmatrix}, \tag{A-4}$$

$$s_{f2} = \begin{pmatrix} 0 & 0 & 0 & 0 & 0 & 0 \\ 0 & K_{N_2} & 0 & K_{NV_2} & 0 & K_{NH_2} \\ 0 & 0 & 0 & 0 & 0 & 0 \\ 0 & K_{NV_2} & 0 & K_{V_2} & 0 & K_{VH_2} \\ 0 & 0 & 0 & 0 & 0 & 0 \\ 0 & K_{NH_2} & 0 & K_{VH_2} & 0 & K_{H_2} \end{pmatrix}. \tag{A-5}$$

The compliance matrix of the isotropic background can be written as

$$s_b = \begin{pmatrix} E^{-1} & -\nu/E & -\nu/E & 0 & 0 & 0 \\ -\nu/E & E^{-1} & -\nu/E & 0 & 0 & 0 \\ -\nu/E & -\nu/E & E^{-1} & 0 & 0 & 0 \\ 0 & 0 & 0 & \mu^{-1} & 0 & 0 \\ 0 & 0 & 0 & 0 & \mu^{-1} & 0 \\ 0 & 0 & 0 & 0 & 0 & \mu^{-1} \end{pmatrix}, \tag{A-6}$$

where E is Young's modulus and ν is Poisson's ratio, which can be expressed through the Lamé parameters λ and μ:

$$E = \frac{\mu\,(3\lambda + 2\mu)}{\lambda + \mu}\,; \tag{A-7}$$

$$\nu = \frac{\lambda}{2\,(\lambda + \mu)}\,. \tag{A-8}$$

APPENDIX B

LINEARIZED STIFFNESS MATRIX FOR TWO ORTHOGONAL FRACTURE SETS

Wave phenomena are more conveniently described using the effective stiffness matrix that can be obtained by inverting the compliance matrix A-2. To obtain weak-anisotropy approximations for seismic signatures, the stiffness elements can be linearized in the normalized quantities called fracture weaknesses. Following Grechka et al.

(2003), the weaknesses for our model can be defined as

$$\Delta_{N_i} \equiv \frac{(\lambda + 2\mu)\, K_{N_i}}{1 + (\lambda + 2\mu)\, K_{N_i}}\,, \tag{B-1}$$

$$\Delta_{V_i} \equiv \frac{\mu K_{V_i}}{1 + \mu K_{V_i}}\,, \tag{B-2}$$

$$\Delta_{H_i} \equiv \frac{\mu K_{H_i}}{1 + \mu K_{H_i}}\,, \tag{B-3}$$

$$\Delta_{NV_i} \equiv \frac{\sqrt{\mu\,(\lambda + 2\mu)} K_{NV_i}}{1 + \sqrt{\mu\,(\lambda + 2\mu)} K_{NV_i}}\,, \tag{B-4}$$

$$\Delta_{NH_i} \equiv \frac{\sqrt{\mu\,(\lambda + 2\mu)} K_{NH_i}}{1 + \sqrt{\mu\,(\lambda + 2\mu)} K_{NH_i}}\,, \tag{B-5}$$

$$\Delta_{VH_i} \equiv \frac{\sqrt{\mu\,(\lambda + 2\mu)} K_{VH_i}}{1 + \sqrt{\mu\,(\lambda + 2\mu)} K_{VH_i}}\,, \tag{B-6}$$

where the subscript $i = 1, 2$ refers to the number of the fracture set. Since the matrix $\mathbf{K}$ has to be nonnegative definite, the weaknesses satisfy the inequalities

$$\Delta_{IJ}^2 \leq \Delta_I\, \Delta_J\,, \tag{B-7}$$

where I and J denote the subscripts N, V, and H.

Using equations A-2 and A-4–A-6 and linearizing the stiffness matrix $\mathbf{c} \equiv \mathbf{s}^{-1}$ in the fracture weaknesses (equations B-1–B-6), we obtain

$$\mathbf{c} \approx \begin{pmatrix} c_{11} & c_{12} & c_{13} & \chi c_{24} & c_{15} & c_{16} \\ c_{12} & c_{22} & c_{23} & c_{24} & \chi c_{15} & c_{26} \\ c_{13} & c_{23} & c_{33} & \chi c_{24} & \chi c_{15} & c_{36} \\ \chi c_{24} & c_{24} & \chi c_{24} & c_{44} & 0 & c_{46} \\ c_{15} & \chi c_{15} & \chi c_{15} & 0 & c_{55} & c_{56} \\ c_{16} & c_{26} & c_{36} & c_{46} & c_{56} & c_{66} \end{pmatrix}\,, \tag{B-8}$$

where

$$\chi \equiv \frac{\lambda}{\lambda + 2\mu} \,. \tag{B-9}$$

The linearized stiffness elements are given by

$$c_{11} = (\lambda + 2\mu) \left(1 - \Delta_{N_1} - \chi^2 \Delta_{N_2}\right) , \tag{B-10}$$

$$c_{12} = \lambda \left(1 - \Delta_{N_1} - \Delta_{N_2}\right) , \tag{B-11}$$

$$c_{13} = \lambda \left(1 - \Delta_{N_1} - \chi \, \Delta_{N_2}\right) , \tag{B-12}$$

$$c_{14} = -\sqrt{\lambda\mu\chi} \, \Delta_{NV_2} \, , \tag{B-13}$$

$$c_{15} = -\sqrt{\mu \left(\lambda + 2\mu\right)} \, \Delta_{NV_1} \, , \tag{B-14}$$

$$c_{16} = -\sqrt{\mu \left(\lambda + 2\mu\right)} \, \left(\Delta_{NH_1} + \chi \, \Delta_{NH_2}\right) , \tag{B-15}$$

$$c_{22} = (\lambda + 2\mu) \left(1 - \Delta_{N_2} - \chi^2 \Delta_{N_1}\right) , \tag{B-16}$$

$$c_{23} = \lambda \left(1 - \chi \, \Delta_{N_1} - \Delta_{N_2}\right) , \tag{B-17}$$

$$c_{24} = -\sqrt{\mu \left(\lambda + 2\mu\right)} \, \Delta_{NV_2} \, , \tag{B-18}$$

$$c_{25} = -\sqrt{\lambda\mu\chi} \, \Delta_{NV_1} \, , \tag{B-19}$$

$$c_{26} = -\sqrt{\mu \left(\lambda + 2\mu\right)} \, \left(\chi \, \Delta_{NH_1} + \Delta_{NH_2}\right) , \tag{B-20}$$

$$c_{33} = (\lambda + 2\mu) \left[1 - \chi^2 \left(\Delta_{N_2} + \Delta_{N_1}\right)\right] , \tag{B-21}$$

$$c_{34} = -\sqrt{\lambda\mu\chi} \, \Delta_{NV_2} \, , \tag{B-22}$$

$$c_{35} = -\sqrt{\lambda\mu\chi} \, \Delta_{NV_1} \, , \tag{B-23}$$

$$c_{36} = -\sqrt{\lambda\mu\chi} \, \left(\Delta_{NH_1} + \Delta_{NH_2}\right) , \tag{B-24}$$

$$c_{44} = \mu \left(1 - \Delta_{V_2}\right) , \tag{B-25}$$

$$c_{45} = 0 \, , \tag{B-26}$$

$$c_{46} = -\mu \sqrt{\frac{\mu}{\lambda + 2\mu}}\, \Delta_{VH_2}\,, \tag{B-27}$$

$$c_{55} = \mu\,(1 - \Delta_{V_1})\,, \tag{B-28}$$

$$c_{56} = -\mu \sqrt{\frac{\mu}{\lambda + 2\mu}}\, \Delta_{VH_1}\,, \tag{B-29}$$

$$c_{66} = \mu\,(1 - \Delta_{H_1} - \Delta_{H_2})\,. \tag{B-30}$$

If the weaknesses of the second fracture set are equal to zero, the linearized effective stiffnesses given above reduce to those obtained by Grechka et al. (2003) for a single microcorrugated fracture set orthogonal to the x_1-axis. Another special case is that of rotationally invariant fractures, for which the off-diagonal weaknesses vanish and the tangential weaknesses Δ_{V_i} and Δ_{H_i} are equal to each other. If both fracture sets are made rotationally invariant, our stiffness matrix becomes identical to that in Bakulin et al. (2000b).

REFERENCES

Bakulin, A., V. Grechka, and I. Tsvankin, 2000a, Estimation of fracture parameters from reflection seismic data - Part I: HTI model due to a single fracture set: Geophysics, **65**, 1788–1802.

——— 2000b, Estimation of fracture paramenters from reflection seismic data - Part II: Fractured models with orthorhombic symmetry: Geophysics, **65**, 1803–1817.

——— 2000c, Estimation of fracture paramenters from reflection seismic data - Part III: Fractured models with monoclinic symmetry: Geophysics, **65**, 1818–1830.

Cardona, R., 2002, Fluid substitution theories and multicomponent seismic characterization of fractured reservoirs: PhD thesis, Colorado School of Mines.

DeVault, B., T. L. Davis, I. Tsvankin, R. Verm, and F. Hilterman, 2002, Multicomponent AVO analysis, Vacuum field, New Mexico: Geophysics, **67**, 701–710.

Farra, V., 2001, High-order perturbations of the phase velocity and polarization of qP and qS waves in anisotropic media: Geophysical Journal International, **147**, 93–104.

Grechka, V., A. Bakulin, and I. Tsvankin, 2003, Seismic characterization of vertical fractures described as general linear-slip interfaces: Geophysical Prospecting, **51**, 117–129.

Grechka, V., P. Contreras, and I. Tsvankin, 2000, Inversion of normal moveout for monoclinic media: Geophysical Prospecting, **48**, 577–602.

Grechka, V. and I. Tsvankin, 2003, Feasibility of seismic characterization of multiple sets: Geophysics, **68**, 1399–1407.

Grechka, V., I. Tsvankin, and J. K. Cohen, 1999, Generalized Dix equation and analytic treatment of normal-moveout velocity for anisotropic media: Geophysical Prospecting, **47**, 117–148.

Gurevich, B., 2003, Elastic properties of saturated porous rocks with aligned fractures: Journal of Applied Geophysics, **54**, 203–218.

Hood, J. A., 1991, A simple method for decomposing fracture-induced anisotropy: Geophysics, **56**, 1275–1279.

Jech, J. and I. Pšenčik, 1989, First-order perturbation method for anisotropic media: Geophysical Journal International, **99**, 369–376.

Kachanov, M. and I. Sevostianov, 2005, On quantitative characterization of microstructures and effective properties: International Journal of Solids and Structures, **42**, 309–336.

Lynn, H., K. M. Simon, M. Layman, R. Schneider, C. R. Bates, and M. Jones, 1995, Use of anisotropy in P-wave and S-wave data for fracture characterization in a naturally fractured gas reservoir: The Leading Edge, **14**, 887–893.

Mallick, S., K. L. Craft, L. J. Meister, and R. E. Chambers, 1998, Determination of the principal directions of azimuthal anisotropy from P-wave seismic data: Geophysics, **63**, 692–706.

Nakagawa, S., K. T. Nihei, and L. R. Myer, 2000, Shear-induced conversion of seismic waves across single fractures: International Journal of Rock Mechanics and Mining Sciences, **37**, 203–218.

Pérez, M. A., V. Grechka, and R. J. Michelena, 1999, Fracture detection in a carbonate reservoir using a variety of seismic methods: Geophysics, **64**, 1266–1276.

Pšenčik, I. and V. Vavryčuk, 2002, Approximate relation between the ray vector and the wave normal in weakly anisotropic media: Studia Geophysica et Geodaetica, **46**, 793–807.

Sayers, C. M. and M. Kachanov, 1995, Microcrack-induced elastic wave anisotropy: Journal of Geophysical Research, **100**, 4149–4156.

Schoenberg, M., 1980, Elastic wave behavior across linear slip interfaces: Journal of the Acoustical Society of America, **68**, 1516–1521.

Schoenberg, M. and J. Douma, 1988, Elastic wave propagation in media with parallel fractures and aligned cracks: Geophysical Prospecting, **36**, 571–590.

Schoenberg, M. and F. Muir, 1989, A calculus for finely layered anisotropic media: Geophysics, **54**, 581–589.

Schoenberg, M. and C. M. Sayers, 1995, Seismic anisotropy of fractured rock: Geophysics, **60**, 204–211.

Thomsen, L., 1988, Reflection seismology over azimuthally anisotropic media: Geophysics, **53**, 304–313.

Tsvankin, I., 2001, Seismic signatures and analysis of reflection data in anisotropic media: Elsevier Science, Inc.

Vavryčuk, V. and I. Pšenčik, 1998, PP-wave reflection coefficients in weakly anisotropic elastic media: Geophysics, **63**, 2129–2141.

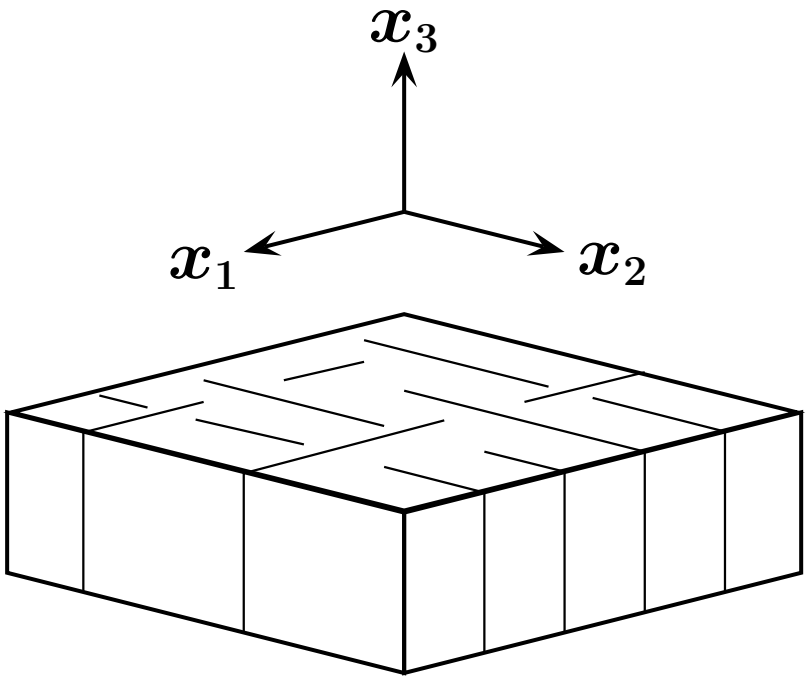

Figure 1: Model of two sets of orthogonal vertical fractures. Since the linear-slip theory does not account for the interaction of fracture sets, fractures are not supposed to intersect each other. The parameters of the fracture set with the normal parallel to the x_1-axis are denoted by the subscript "1" in the text.

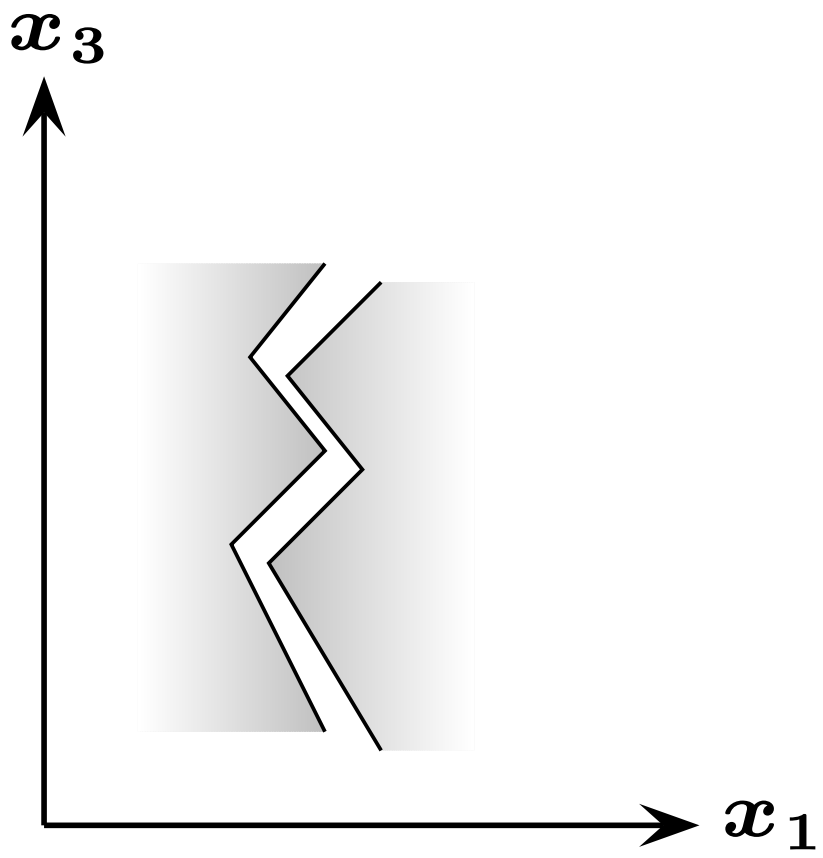

Figure 2: Idealized fracture with corrugations that are offset from one face to the other (adapted from Schoenberg and Douma, 1988). In such a model, the normal slips (discontinuities in displacement) are coupled to the shear stresses and vice-versa. For example, slip in the x_3-direction will cause the coupling of the fracture faces and, therefore, shear stress in the x_1-direction.

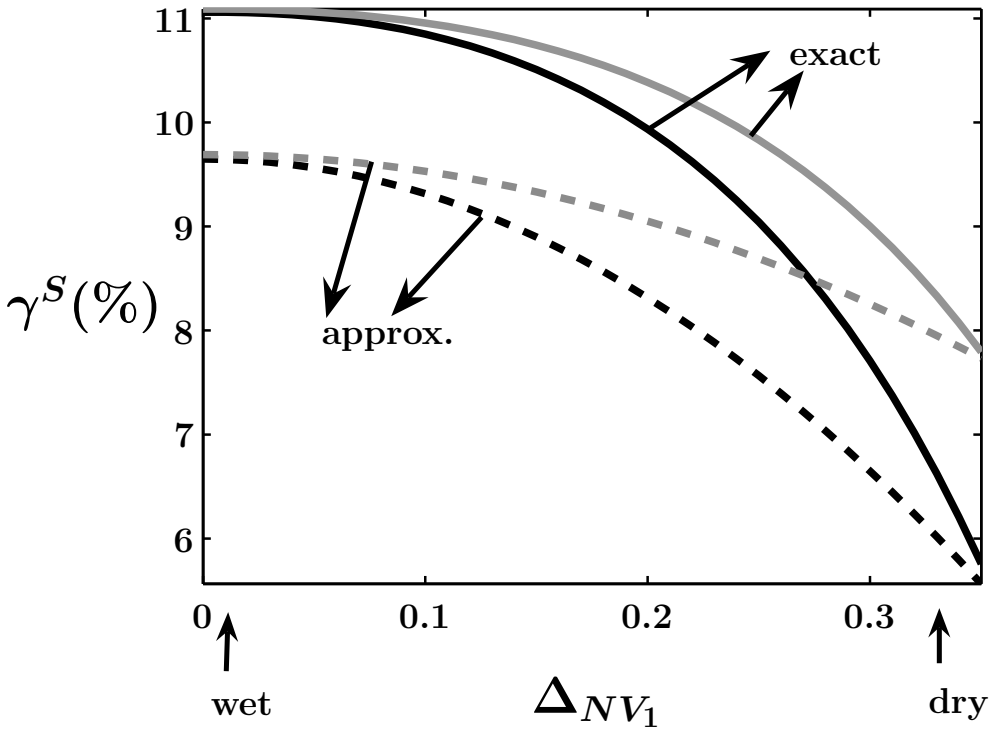

Figure 3: Variation of the shear-wave splitting coefficient (γ^S) for vertical propagation as a function of the weakness Δ_{NV_1} and the V_{Pb}/V_{Sb} ratio. The solid curves mark the exact γ^S from equation 11, where the velocities are computed from the Christoffel equation; the dashed curves are the approximation 12. The V_{Pb}/V_{Sb} ratio is equal to two (black lines) and three (gray). The other model parameters are $V_{Pb} = 3$ km/s, $\Delta_{N_1} = 0.5$, $\Delta_{V_1} = \Delta_{H_1} = 0.25$, and $\Delta_{NH_1} = \Delta_{VH_1} = 0.1$. Each weakness of the second fracture set except for Δ_{NV_2} is equal one-third of the corresponding weakness of the first set; $\Delta_{NV_2} = (1/3)\Delta_{NH_1}$.

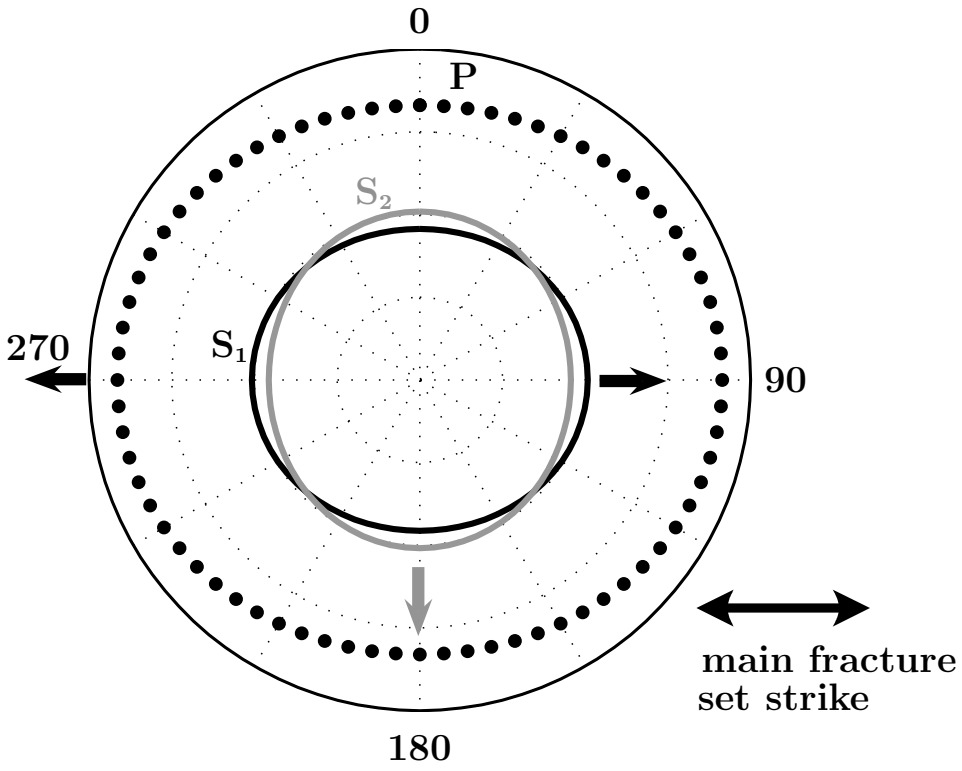

Figure 4: Exact NMO ellipses of P-waves (dotted), S_1-waves (solid black) and S_2-waves (solid gray) for an effective orthorhombic model formed by two vertical, orthogonal sets of rotationally invariant fractures. The semi-major axes (black arrows) of the P- and S_1-wave NMO ellipses are parallel to the strike of the dominant fractured set (azimuth 90°). The semi-major axis of S_2-wave ellipse (gray arrow) is orthogonal to the main fracture set. The parameters are $V_{Pb} = 2$ km/s, $V_{Sb} = 1$ km/s, $\Delta_{N_1} = 0.25$, and $\Delta_{V_1} = \Delta_{H_1} = 0.12$. Each weakness of the second fracture set is equal to one-third of the corresponding weakness of the first set. The radius of the external circle corresponds to 2 km/s.

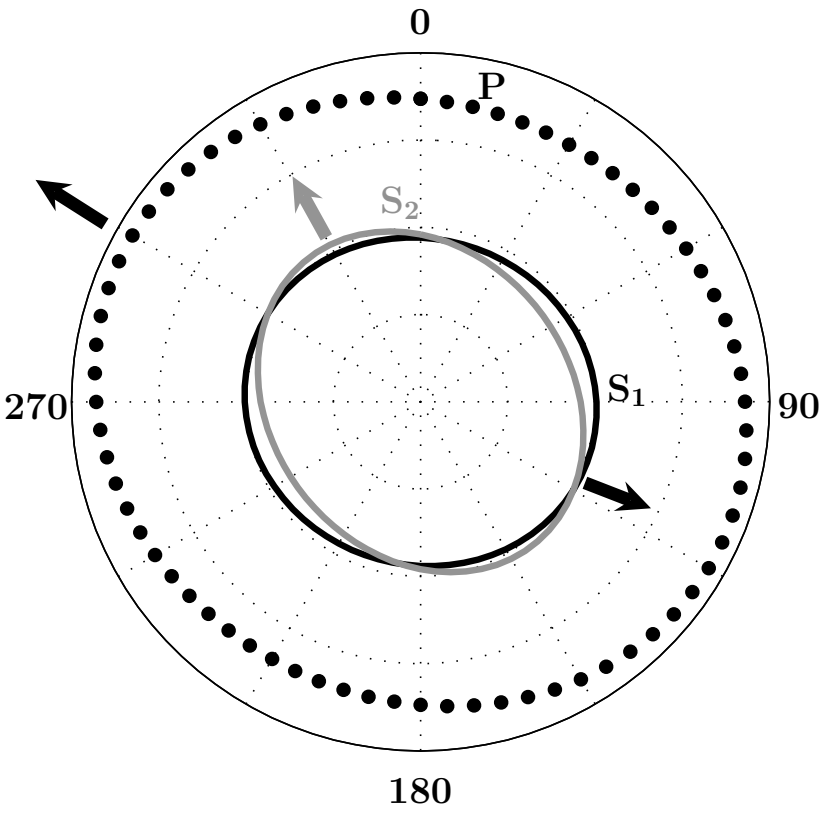

Figure 5: Exact NMO ellipses for two vertical, orthogonal sets of microcorrugated fractures. The strike azimuth of the dominant (first) fracture set is 90°. The parameters are V_{Pb}=2 km/s, V_{Sb}=1 km/s, $\Delta_{N_1} = 0.25$, $\Delta_{V_1} = \Delta_{H_1} = 0.12$, $\Delta_{NV_1} = \Delta_{NH_1} = 0.17$, and $\Delta_{VH_1} = 0.12$. Each weakness of the second fracture set is equal to one-third of the corresponding weakness of the first set.

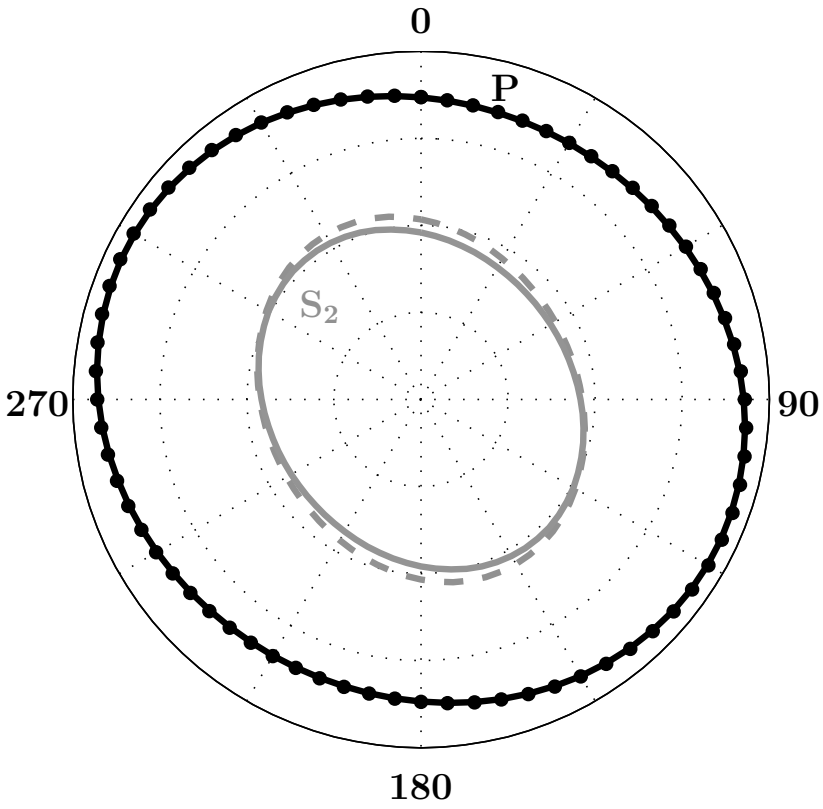

Figure 6: Comparison between the exact NMO ellipses of the P- and S_2-waves from Figure 5 (solid lines) and the weak-anisotropy approximations (dots for the P-wave and the dashed line for the S_2-wave). The approximations are computed from equations 17–19 and 29–31. The exact and approximate NMO ellipses of the S_1-wave (not shown) practically coincide with each other.

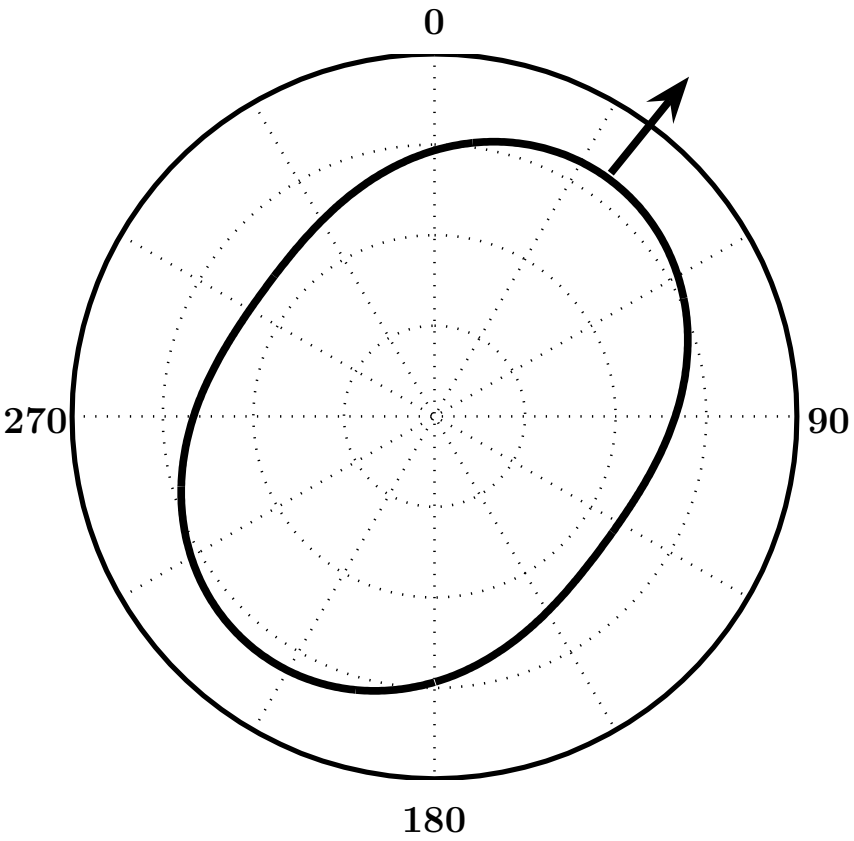

Figure 7: Azimuthal variation of the absolute value of the P-wave AVO gradient for our triclinic model computed from equation 37. The strike azimuth of the dominant fracture set is 90°; the direction of the largest gradient (black arrow) is close to 35°. The parameters are $V_{Pb}/V_{Sb} = 3$, $\Delta_{N_1} = 0.25$, $\Delta_{V_1} = \Delta_{H_1} = 0.12$, and $\Delta_{NH_1} = 0.05$. Each weakness of the second fracture set is equal to one-third of the corresponding weakness of the first set.